

Disclosing residual thermal stresses in UHT fibre-reinforced ceramic composites and their effect on mechanical behaviour and damage evolution

Pietro Galizia*, Diletta Sciti

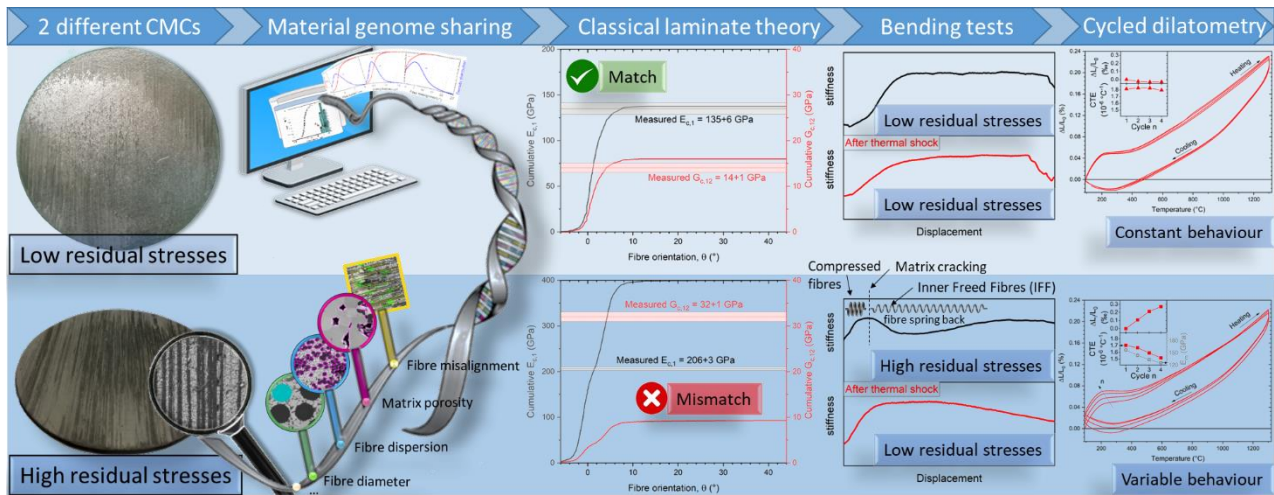
National Research Council, Institute of Science and Technology for Ceramics, Via Granarolo 64, 48018 Faenza, Italy

*Corresponding author. e-mail: pietro.galizia@istec.cnr.it

Abstract

Reusability of CMCs with inherently high temperature capabilities and ablation resistance goes through the understanding of the effects of residual thermal stresses (RTS) caused by thermal expansion mismatch between fibre and matrix. In this work, RTSs of carbon fibre-reinforced ultra-high temperature ZrB₂-SiC based ceramic were tailored through fibre anisotropy and fibre coating. A detailed microstructural analysis about the state of matrix (i.e. residual porosity and cracks) and fibre (i.e. intra fibre bundles porosity, fibre volumetric content and its degree of dispersion) was performed. The different RTS level, among the composites, was investigated by comparing stiffness-displacement curves of bending test and cycled dilatometric curves. The correlation between RTS level and thermomechanical behaviour was also assessed through bending test at 1500°C and after thermal shock. The results showed that RTSs not only reduced the flexural strength, but also influenced the damage evolution and the stiffness linearity. As a consequence, RTSs releasing can alter not only the pristine geometry, achieved after sintering or machining, due to the formation of inner freed fibres (IFFs) but also the matrix Young's modulus and the stress and strain at failure onset of the investigated CMCs.

Graphical abstract



Keywords: A. Ceramic-matrix composites (CMCs); B. Residual/internal stress; C. Damage mechanics; D. Mechanical testing; Material genome.

1 Introduction

The driving force to develop reusable launch vehicles (RLV) is the awaited reduction of the refurbishing costs, which are attested around 30% of manufacturing costs and provides more opportunities for service missions [1,2]. Required materials for RLVs should not suffer operating temperatures higher than 1700 °C [3]. This requirement would also lead to the increase of the efficiency of the propulsion systems and the durability of the thermal protection systems (TPS) [4,5]. Ultra-high ceramic matrix composites (UHTCMC) are emerging as promising candidates to develop RLVs because they merge their intrinsic temperature capabilities with the needed structural properties [6–12]. This novel class of CMCs [13,14] showed unprecedented ablation and oxidation resistance [15–17] and strength-toughness combination [18,19], and is overturning the common criterion: CMCs cannot be densified without losing damage tolerance [20]. However, the integration of fibres within the dense matrix through sintering can lead to the accumulation of RTSS during the cooling phase of the consolidation process, and the evolution of damage and stiffness of the components under operational thermal cycles [21]. The reason lies on the coefficient of thermal expansion mismatch between longitudinal axis of the carbon fibre (CTE ranges from $-1.5 \cdot 10^{-6} \text{ }^{\circ}\text{C}^{-1}$ at RT to $1.4 \cdot 10^{-6} \text{ }^{\circ}\text{C}^{-1}$ at 1500 °C [22]) and the $\text{ZrB}_2\text{-SiC}$ based matrix (if CTE of the matrix is assumed to be similar to that of polycrystalline ZrB_2 [23], CTE ranges from $5.2 \cdot 10^{-6} \text{ }^{\circ}\text{C}^{-1}$ at RT to $8.7 \cdot 10^{-6} \text{ }^{\circ}\text{C}^{-1}$ at 1500 °C). Hence, according to Ref.s [22,23], $\Delta|\text{CTE}|$ ranges between $6.7 \cdot 10^{-6} \text{ }^{\circ}\text{C}^{-1}$ and $7.6 \cdot 10^{-6} \text{ }^{\circ}\text{C}^{-1}$ in the temperature

range from RT to 1500 °C. Pyrolytic carbon coating and matrix porosity are considered key microstructural parameters affecting the mechanical properties of the as produced components [24–28] since they also control the RTSs on the fibre/matrix interface [19,29–32]. Understanding the role of RTSs in the thermomechanical behaviour and damage evolution of UHTCMCs is of paramount importance to push their application in RLVs [21,33–38]. Recently, Wang et al. [32] and Chen et al. [39] showed that the damage induced by the initial RTSs can be tailored through the thickness of the PyC coating and matrix layer thickness, respectively. The increase of cracks density, proportional to the thickness of the PyC coating, on one hand, relieved the stress, on the other hand, reduced the stiffness of the material. A first study on highly stressed UHTCMC [21], consolidated in hot press by reactive sintering at 1900 °C and characterized by 45 vol% of uncoated pitch carbon fibre and 7 vol% of pores, showed that thermal cycles led to (i) matrix cracking, (ii) decrease of matrix modulus, and (iii) an overall thermal dilatation of the composite that gradually approached that of bare carbon fibre.

In this work, we addressed the following questions: (i) how, and whether, RTSs and thermal damage in sintered UHTCMCs can be controlled by changing microstructural characteristics; and (ii) whether the level of RTSs has an in-operating impact on the structural properties. To answer the above raised points, two UHTCMCs based on ZrB₂-SiC based matrix reinforced with continuous carbon fibre and characterized by different level of RTSs were fabricated. Intermediate modulus PAN-derived fibres (tensile modulus and CTE according to the supplier are 294 GPa and $-0.4 \cdot 10^{-6} \text{ }^{\circ}\text{C}^{-1}$, respectively) coated with pyrolytic carbon (PyC) were used to fabricate slightly stressed UHTCMCs. In contrast, the level of RTSs was maximized by using uncoated ultra-high modulus pitch-derived fibres (tensile modulus and CTE according to the supplier are 780 GPa and $-1.5 \cdot 10^{-6} \text{ }^{\circ}\text{C}^{-1}$, respectively). Microstructural characteristics were reported as cumulative distribution functions and used in the classical laminate theory to calculate the expected Young's and shear moduli. The thermomechanical behaviour of the composites was investigated through a deep analysis of those tests that affect the residual stress level, e.g. (i) flexural strength tests at room temperature before and after thermal shock at 1500°C, (ii) flexural strength tests at 1500°C, (iii) cycled dilatometric analysis. These thermomechanical tests and their comparison allowed to probe the RTS and observe their effect on the mechanical behaviour and damage evolution.

2 Experimental

2.1 Material manufacturing

Water-based slurry containing a 90 vol.% ZrB_2 –10 vol.% SiC powder mixture was used to manually impregnate the pitch-derived preforms (XN80-6K, Granoc, Japan) In parallel, the same slurry was used to wet PyC-coated PAN-derived carbon fibres that were unidirectionally woven through filament winding (T800HB-6000, TORAYCA, Japan). Then, impregnated layers of both types of unidirectional (UD) preforms were overlapped in 0/0° stacking sequence to get UD composites. The samples, in agreement with the kind of reinforcing fibre, were named PAN and PITCH in the following. Green samples were then sintered by spark plasma sintering under vacuum at 1850 °C, with 200 s holding time, 100 °C/min heating rate and 40 MPa applied pressure. Further details on the process were reported in the previously published works [19][31][40].

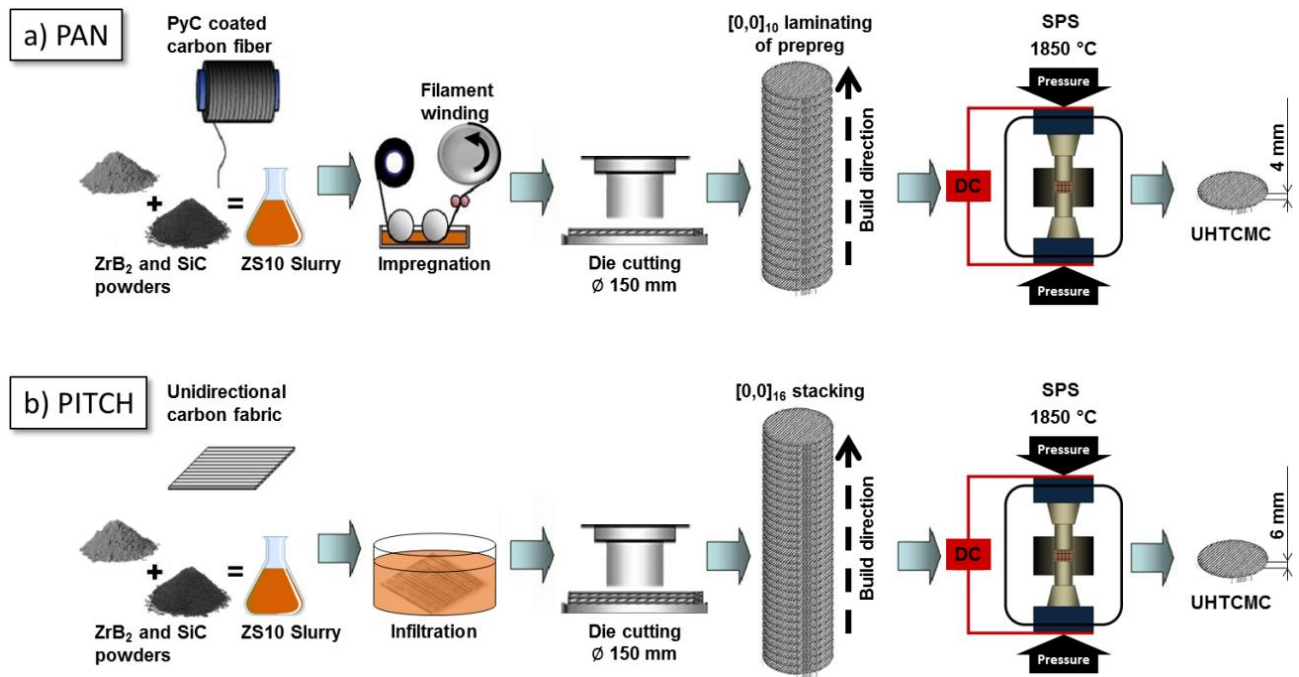


Fig.1 Schematic flowchart of a) filament winding and sintering process and b) slurry infiltration and sintering process to manufacture PAN and PITCH UHTCMCs, respectively.

2.2 Microstructural characterization

The density (ρ) was measured through geometrical method on five grinded pellets of about 5 g and dimensions and parallelism tolerances smaller than 0.1 mm. The relative density ($\rho_{\%}$) of the composites was calculated as ratio between the measured density (ρ) and the theoretical density (ρ_{th}), where ρ_{th} was calculated by multiplying the measured volumetric

fraction of each phase by its theoretical density: 6.10 g/cm³ of ZrB₂; 3.21 g/cm³ of SiC; 2.20 g/cm³ of PyC; 1.80 g/cm³ of PAN-C_f; 2.17 g/cm³ of PITCH-C_f.

The microstructures were analysed on polished and fractured surfaces using field emission scanning electron microscopy (FE-SEM, Carl Zeiss Sigma NTS GmbH Oberkochen, Germany). Image analysis (Image-Pro Analyzer 7.0, v.7, Media Cybernetics, USA) on micrographs of polished sections was performed to measure: fibre diameter (D); thickness of fibre coating (T); size of cavities between fibre and coating (p_i); fibres bundle area (B); size of intrabundle voids (p_b); size of residual matrix porosity (p_m); crack spacing (S); fibre misalignment (θ) and volumetric content of fibre (C_f), coating (PyC), ZrB₂, SiC, residual porosity within the matrix (i.e. degree of matrix densification), intrabundle voids (i.e. degree of slurry infiltration), and cavities between fibre and coating. The size of D, p_i, p_b and p_m was calculated as equivalent circular area diameter. T was calculated as half the difference between equivalent circular area diameter of the coated fibre and that of the fibre without considering the coating. B was calculated by summing the areas of contacted fibres. It was considered that a bundle is formed when two or more neighbour fibre are in contact. If one fibre is not in contact with another, B corresponds to the area of that fibre. Consequently, the more B values equal to that of a single fibre, the more dispersed the fibres are. Furthermore, it is possible estimate the number of fibres of the bundles simply dividing the bundle area per the mean fibre area. The volumetric contents related to fibres and matrix features were measured on a surface of at least 2.5 mm² and 2500 μm², respectively. The cumulative distribution functions (CDF) of the microstructural features, measured through image analysis, were fitted using one of the two equations below to obtain R² > 0.99 [41]:

$$F(x) = 1 + \frac{p_1(1+b_1)}{1+e^{-\frac{x-x_1}{a_1}}} + b_2 + \frac{(1-p_1)}{1+e^{-\frac{x-x_2}{a_2}}} \quad (1)$$

$$F(x) = 1 + \frac{(1+b_1)}{1+\left(\frac{x}{x_1}\right)^{a_1}} \quad (2)$$

Where x is the generic microstructural quantity (D, T, p_i, B, p_b, p_m, S), x₁ and x₂ are the corresponding median values (50th percentile) of, at most, two intended populations and p₁ is the fraction of the first population. It is worth noting that the extrapolated parameter values and their probably distribution functions are useful for the modelling, where the uncertainty of microstructural features is becoming increasingly important [28,32,41–46]. Moreover these extrapolated parameter offer an initial microstructural genome [47] of the investigated materials, which is useful for dissemination purpose and facilitation of

discovery and design of this class of composites.

2.3 Thermomechanical characterization

Longitudinal Young's modulus (E_1) and transverse shear modulus (G_{23}) of the as produced unidirectional composites were measured through sonic resonance method (ASTM E1875–08).

Flexural tests were performed on 25 mm × 2.5 mm × 2.0 mm bars (length by width by thickness, respectively) using a four-point fixture with an upper span of 10 mm and a lower span (s) of 20 mm, and a crosshead speed of 1 mm/min. The bars were tested at:

- RT in both longitudinal and transversal directions (σ_1 and σ_2 , respectively);
- RT after thermal shock through water-quenching from 1500 °C to 20 °C of bath temperature (only longitudinal bars, $\sigma_1^{\Delta T}$);
- at 1500 °C in Ar atmosphere (only longitudinal bars, $\sigma_1^{1500^\circ\text{C}}$).

For each test, three bars were used. Further details of experimental method are reported in Ref.[48]. Both displacement and calculated stiffness (the slope of the load-displacement curve) were normalized in order to better compare the slope variations among the load–displacement curves and because it is hard to evaluate them in quantitative terms [46]. In particular, the stiffness was normalized by its maximum value and the displacement was divided by the value of the displacement at the maximum applied load. This relative displacement (D_F) should be intended as the displacement to failure that occurs when $D_F = 100\%$. However, strain values (ε) were calculated according to the following equation:

$$\varepsilon = 4.36 \frac{Dd}{s^2} \quad (3)$$

where d is the average test specimen thickness and D is the deflection at beam centre at a given point in the test.

Flexural strength at RT along the longitudinal direction was measured on larger specimens of 60 mm × 10 mm × 2.5 mm (length by width by thickness, respectively) using a three-point fixture with s = 50 mm, and a crosshead speed of 8 mm/min. These tests were performed in order to assess the degree of interlaminar shear contribution to the failure and measure a more reliable strength value [41].

The relative dimensional change ($\Delta L/L_0$) vs. temperature was recorded along the longitudinal direction during 4 consecutive cycles from about 90°C up to 1300 °C under flowing argon of 100 ml/min and 10 °C/min heating rate. The coefficient of thermal expansion (α_1^n , where n superscript is an integer number indicating the number of the thermal cycle) was calculated as the slope of the secant line joining the values at 100 °C and 1300 °C. Further experimental details are reported in Ref. [21].

3 Results and discussion

3.1 Results and novelties of microstructural characterization of UHTCMCs

Typical microstructures of sintered PAN and PITCH composites are illustrated in Fig. 2. The first differences that stand out were the partially uneven fibre distribution in the sample PAN and its higher amount of volumetric PyC/C_f content with respect to the sample PITCH. As designed, experimental density and residual porosity were quite different between the two composites and confirmed the higher densification of PITCH material, with 3.55 g/cm³ of density and 8 vol% of overall porosity, compared to PAN material, which was characterized by 2.76 g/cm³ of density and 18 vol% of overall porosity (see Table 1). The uneven fibre distribution and the higher amount of coated fibre and pores of PAN composite should be mainly ascribed to the PyC-coating procedure, that partially stucked the fibres each other making the slurry infiltration difficult. As a result, PAN composite had a lower matrix volumetric content with respect to PITCH composite, 28 vs 41%, and higher residual porosity, 9 vs 6 %. Different types of porosity (p_i , p_b and p_m) were analysed (see Table 1). The distinction of the different types of porosity is of paramount importance for the development and design of UHTCMCs. In fact, the above porosities are mainly due to different process steps: p_i to PyC-coating procedure, p_b to slurry infiltration as consequence of missed slurry penetration and p_m to sintering. These porosities were found to differentially affect structural properties and environmental resistance. In the present case, it was found that PAN material was characterized by a widespread porosity both inside the fibre bundles and the matrix, which in both cases was higher than that of PITCH material.

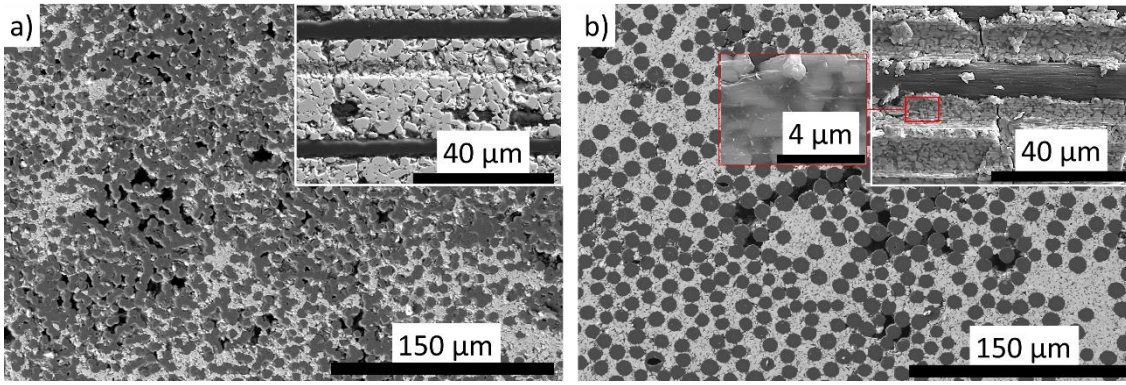


Fig.2 SEM micrographs of the polished surfaces perpendicular to the fibre axis of (a) PAN and (b) PITCH materials. The light grey areas and the black areas correspond to the matrix and pores, respectively. The dark grey areas correspond to PyC coated Toray T800 fibre in the case of PAN material and to the Granoc XN80 fibre in case of PITCH material. The insets show the surfaces parallel. The zoom of the inset (b) shows the graphite layers stuck to the matrix after intra-fibre debonding.

Table. 1 Values of density (ρ), relative density ($\rho_{\%}$) and volume percent contents of phases: carbon fibre (C_f); pyrolytic carbon (PyC), cavities between fibre and coating (p_i); intrabundle voids (p_b); ZrB₂, SiC and residual matrix porosity (p_m); longitudinal flexural strength (σ_1); transverse flexural strength (σ_2); Young's modulus (E_1); shear modulus (G_{12}); linear coefficient of thermal expansion (α_1). The percentage values were rounded to nearest integer.

ID	Composite		Fibre				Matrix			Mechanical properties				CTE
	ρ	$\rho_{\%}$	C_f	PyC	p_i	p_b	ZrB ₂	SiC	p_m	σ_1	σ_2	E_1	G_{12}	α_1
	g/cm ³	%	vol%							MPa		GPa		10 ⁻⁶ °C ⁻¹
PAN	2.76±0.04	82	34	20	1	8	25	3	9	631±12	25±1	135±6	14±1	1.81
PITCH	3.55±0.05	92	51	-	-	2	37	4	6	329±9	61±13	206±3	32±1	1.70

Fig.s 3 and 4 and Table A.1. (Appendix A) highlight further details of the obtained microstructures.

PAN composite: the median value of fibre diameter and PyC coating thickness was about 5 and 0.6 μm , respectively (Fig. 3a, b). These values are comparable with those observed in UHCTMC composite fabricated starting with the same coated fibre preforms but consolidated through three cycles of polymer infiltration and pyrolysis at 1600 °C in N₂ atmosphere [41]. This suggests that heat treatment through SPS at 1850 °C did not induced any appreciable degradation of the fibres with respect to the PIP process. The absence of internal microstructural changes inside the PAN-derived fibres upon densification at high temperature was also observed through TEM analysis [40]. On the other hand, the applied uniaxial pressure during SPS process could be the cause of cavities observed between fibre and coating (Fig. 3c) absent in PIPed UHTCMCs [41,49].

Fibre clusters, consisting of more than five fibres not fully impregnated and characterized by weak PyC-fibre/PyC-fibre interfaces, were calculated as 63% of the total fibre amount (against the 14% of well dispersed single filaments, Fig.3 d) with an equivalent mean diameter of 19 μm . The pores inside the partially infiltrated bundles represented the 8% of the PAN composite and were on average 3 μm . Fibre angle distribution was characterized by an average offset of 1.5° with respect to the major axis of the bar (Fig.3 f). The distribution is quite narrow and only 5% of the fibres had a misalignment larger than $|6^\circ|$. The misalignment on the top surface (i.e. the surface used as reference during the machining of the specimen) resulted with an average fibre misalignment of almost 0.5° and can be attributed to the misalignment of the cutting tool. On the other hand, the higher misalignment, of about 2.4°, observed in the other surface should be attributed to the manually stacking of the impregnated preforms.

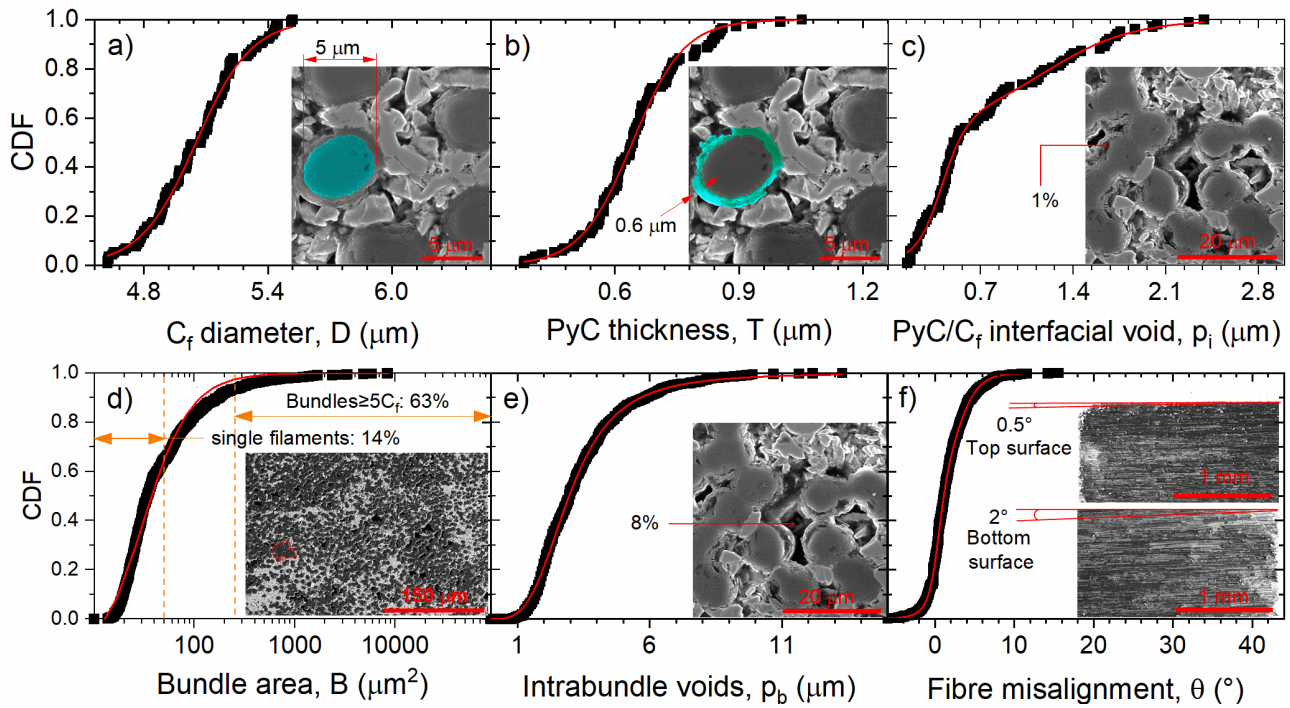


Fig.3. Microstructure of PAN composites depicted as Cumulative Distribution Functions, CDF, of (a) fibre diameter, D , (b) thickness of fibre coating, T , (c) size of cavities between fibre and coating, p_i , (d) area of fibres bundle, B , (e) size of intrabundle voids, p_b and (f) fibre misalignment, θ . Experimental points and fitted CDFs are plotted as black symbols and red line, respectively. The values of parameters of all fitted CDFs are shown in Table A.1.

PITCH composite: no evidence of fibre degradation after heat treatment was found.

Although, chemical reactions between C and oxide phases from ZrB_2 particle surface, e.g.

B_2O_3 and ZrO_2 consume the fibre during sintering at temperature higher than $1500^\circ C$ [23], the CDF of diameter of uncoated pitch-derived fibre (Fig. 4a) well matched that of PIPed composites treated at $1000^\circ C$ in Ar [50] and no appreciable differences were observed in terms of fraction, median values and FWHM of the two populations. Hence, it is reasonable that sintering at high temperature did not affect the fibre performances. Retention of fibre properties after sintering was suggested by previous works on dilatometric curves of a similar composite [21]. Looking at the fibre distribution (Fig. 3b), up to 39% of the fibres were dispersed into the matrix as single filaments characterized by strong interfaces due to mechanical interlocking. Fibre clusters, consisting of more than five fibres not completely impregnated by the slurry and thus characterized by weak fibre/fibre interfaces, were attested to be 30% with an equivalent mean diameter of $28\text{ }\mu m$. The lower porosity inside the partially infiltrated bundles of PITCH composite (Fig. 4c) with respect to the PAN composite (2 vol% vs 8 vol%) should be ascribed to the better slurry infiltration obtained with uncoated fibre. On the other hand, the calculated equivalent diameter of intrabundle pores showed a median value of $5\text{ }\mu m$ and ranged up to $23\text{ }\mu m$ in case of PITCH composite, instead of the median and maximum value of 3 and $14\text{ }\mu m$, respectively, measured in case of PAN composite. This should be attributed to larger diameter of pitch-derived fibres, with respect to that of PAN-derived fibres, as the size of interstitial voids between the close packed fibres is proportional to the fibre diameter. Fibre angle distribution was characterized by an average offset of 2.9° (Fig. 4d). The higher fibre misalignment with respect to PAN composite should be attributed to a larger error made in the machining phase (1.3° instead of 0.5°) and to the manually slurry infiltration instead of filament winding that broadened the distribution: only 87% of the fibres had a misalignment lower than $|6^\circ|$ and more than $|9^\circ|$ was needed to achieve the 95% of the fibres. This broad fibre angle distribution was also due to the larger stacking-fault produced during the lay-up of the infiltrated plies: there were 5° between the two surfaces instead of the 1.5° observed for PAN composite. Looking at the matrix (Fig. 4e), 6 vol% of residual porosity with a median size of $0.4\text{ }\mu m$ was observed. The well sintered grains allowed to observe vertical cracks (perpendicular to the fibre axis direction) spaced $22\text{ }\mu m$ (Fig. 4f). The formation of these inter/trans granular cracks was expected due to coefficient of thermal expansion (CTE) mismatch between matrix and fibre [21]. In fact, the measured spacing matched that of similar composites [20,21].

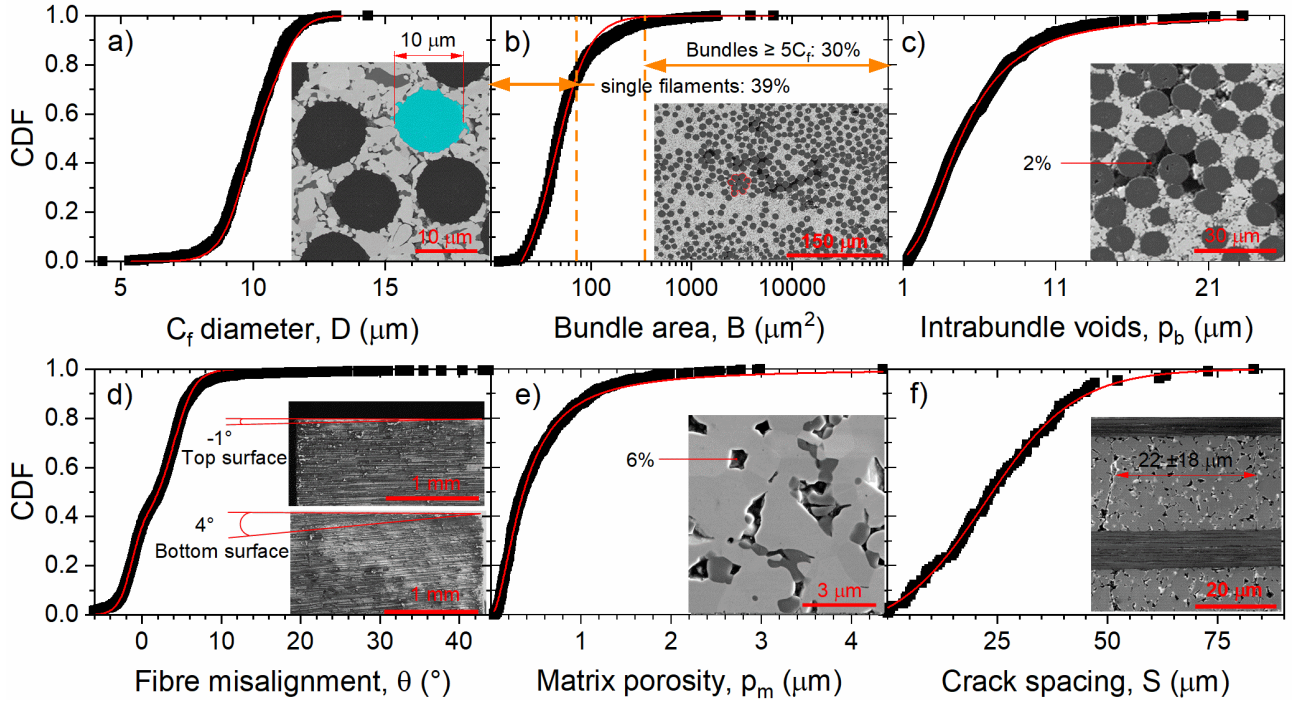


Fig.4. Microstructure of PITCH composites depicted as Cumulative Distribution Functions, CDF, of (a) fibre diameter, D , (b) area of fibres bundle, B , (c) size of intrabundle voids, p_b , (d) fibre misalignment, θ , (e) size of residual matrix porosity, p_m and (f) crack spacing, S . Experimental points and fitted CDFs are plotted as black symbols and red line, respectively. The values of parameters of all fitted CDFs are shown in Table A.1.

3.2 Elastic moduli

The measured Young's modulus and shear modulus of PAN composite was 135 ± 6 and 14 ± 1 GPa, respectively. These values well agree with the expected ones from the classic laminate theory and the measured microstructural characteristics and the moduli of the constituent phases (see appendix B). As for PITCH composite, the calculated range values of the Young's modulus of the matrix agrees with the value of 157 GPa extrapolated from dilatometry (further details on the measurement of matrix modulus are reported in the paragraph 3.5 Cycled dilatometry). However, the measured Young's modulus and shear modulus of 206 ± 3 and 32 ± 1 GPa, respectively, are out of the calculated range. Similar results were obtained in the first study on highly stressed UHTCMC [21] and corroborate that matrix porosity and microcracks, and fibre misalignment angle are not enough to justify the lower Young's modulus and higher shear modulus showed by these highly stressed composites.

3.3 Flexural curves of as produced (i.e. stressed) and thermally shocked (i.e. relaxed) samples

In this section we show that by comparing the flexural curves of PAN and PITCH composites as-produced (AP) and subjected to thermal shock (ΔT) we can extrapolate information about the effect of RTSs on the mechanical behaviour and the different failure sequence of UHTCMCs. This is possible due to the two different microstructures that are designed to have low RTSs (AP-PAN composite) and high RTSs (AP-PITCH composite). For this purpose, the bending curves in Fig.5 (i) are plotted as stress vs normalized displacement up to the point of failure—the whole curves have been presented in previous works [19,31,40]— and (ii) are juxtaposed with the first derivative (i.e. stiffness vs normalized displacement) highlighting the slope and transitions.

For each curve 4 stages were identified:

- 1) "fixture/specimen alignment": this is the typical toe region of the bending curves, caused by a take-up of slack and alignment or seating of the test specimen. In this region, the initial uneven force application gradually disappears as the test fixtures gradually approach the specimen and aligns each other. For this reason, the "fixture/specimen alignment" region is an artifact that should be compensated to find the corrected zero point on the strain.
- 2) "Matrix/fibre stress transmission": it is the stage characterized by a steady increasing of the flexural stiffness up to its maximum value. At this point the load transfer from the matrix is maximized and taut and straightened fibres give their maximum collective response to the applied load.
- 3) "Load-bearing fibres": in this stage the load is mainly sustained by the fibre, and it is extended up to the failure onset.
- 4) "Failure onset": this is identified as the point from which the flexural stiffness starts to steady decrease until the final failure.

Each stage occurred at different ranges of displacement in function of the material and its state (AP or ΔT). To better highlight the extension of these stages, the calculated ranges of microstrain for each stage are plotted as bar chart in Fig.6, while the stress-strain values of each transition are reported in Table C.1 and showed as simplified flexural stress-strain curves in Fig. C.1. A detailed discussion of each step is reported in the following subparagraphs.

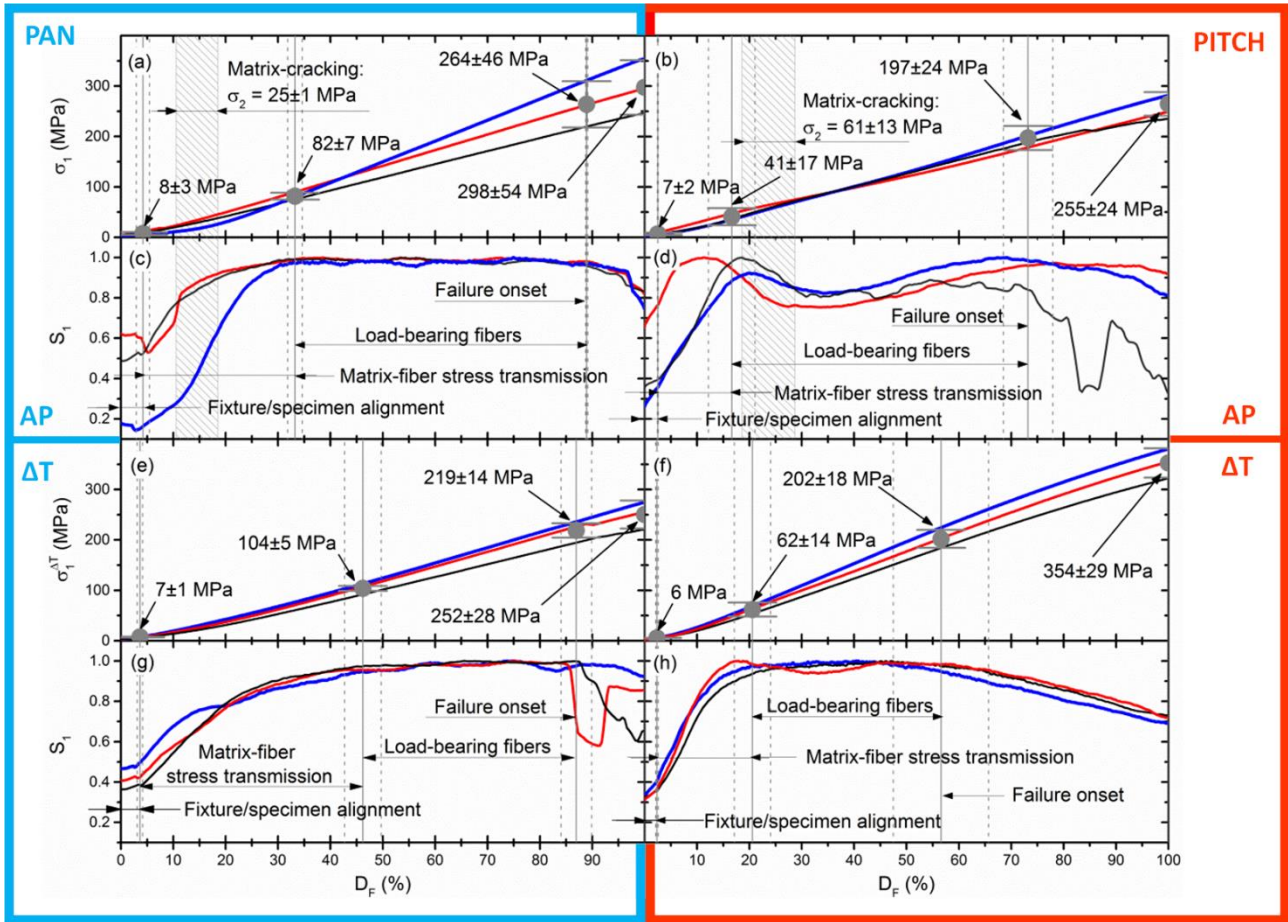


Fig.5. Stress versus displacement to failure (ratio of displacement to its value at the maximum applied load) curves (σ - D_F) of as produced (a) PAN and (b) PITCH composites, and thermally shocked (e) PAN and (f) PITCH composites. From each σ_1 - D_F curve, normalized stiffness (S_1 , ratio of stiffness to its maximum value) was calculated and plotted versus D_F for as produced (c) PAN and (d) PITCH composites, and thermally shocked (g) PAN and (h) PITCH composites. The three solid vertical lines and the related dashed lines represent, respectively, the average values and the standard deviations of D_F at which the transitions: "fixture/specimen alignment", "matrix/fibre stress transmission", "load-bearing fibres" and "failure onset" occurred. Matrix-cracking region, individuated as the strength of the transverse direction [31], was highlighted by filling the area with lines pattern.

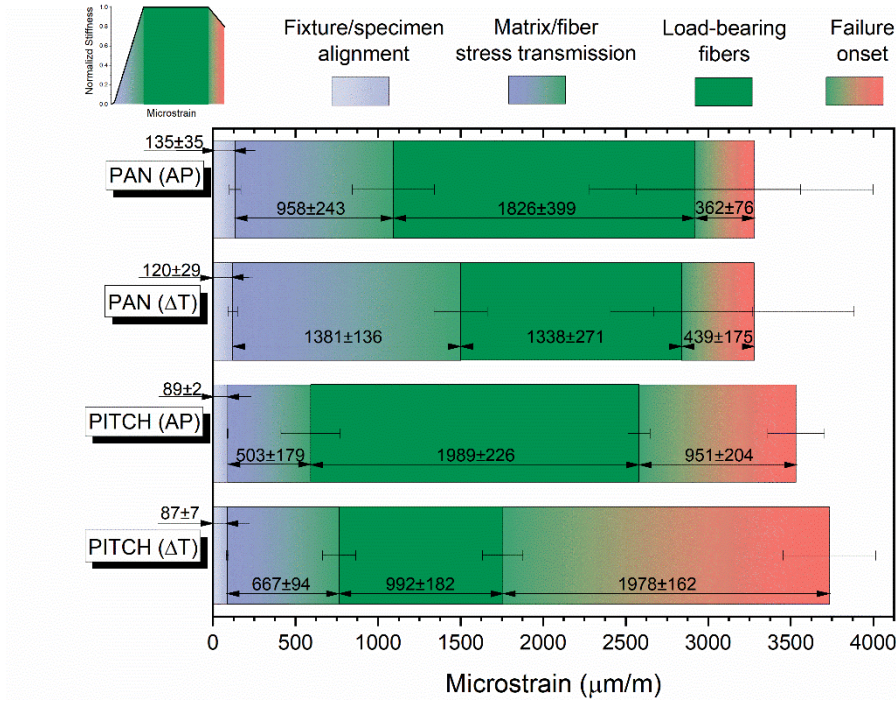


Fig.6. Transition from "fixture/specimen alignment" to "matrix/fibre stress transmission", "load-bearing fibres" and "failure stage" as function of the applied strain during the bending test of the as-produced (AP) and thermally shocked (ΔT) PAN and PITCH samples. In the schematic normalized stiffness vs. strain (showed in the top left corner) each region is highlighted with the same colours used in the bar plot.

3.3.1 Fixture-specimen alignment stage

In the initial stage of loading all curves (Fig.5) present a change of the slope of the stiffness-displacement curve (S_1 - D_F). This variation mainly stemmed from the self-aligning processes between the test fixtures and the specimen and involved a comparable displacement to failure ($D_F = 2$ -4%) and applied stress ($\sigma_1 = 6$ -8 MPa) among all the AP and ΔT composites.

3.3.2 Matrix-fibre stress transmission stage

After the first stage of adjusting, S_1 - D_F curves of AP-PAN specimen showed a non-linear increase of stiffness up to their maximum value, while the trend of AP-PITCH specimens was more linear. This could be due to the different strength of the matrix among the two materials. If the matrix strength is assumed to be the same of the strength of the composites along the transverse direction, the matrix of AP-PAN and AP-PITCH sample should have a strength of 25 and 60 MPa, respectively. Using these values, for AP-PAN specimens the matrix failure fell within the matrix-fibre stress transmission stage (D_F of matrix cracking ranged between 11 and 19%), exactly in correspondence with a strong

change of linearity of the S_1 curves. While, for AP-PITCH specimens the failure matrix ($D_F = 18\text{-}29\%$) coincided with the transition to the next stage and the losing of linearity. Moreover, it can be seen that AP-PAN composites, with respect to AP-PITCH ones, required higher values of σ_1 , D_F and $\mu\varepsilon$ to saturate the load transmission: 82 MPa, 33% and 1093 $\mu\text{m/m}$, instead of 41 MPa, 17% and 592 $\mu\text{m/m}$. The higher stress transmit capacity of AP-PITCH specimens should be ascribed to the absence of PyC coating, to the better fibre dispersion (less amount of fibre bundles and intrabundles pores) and to the higher matrix densification that formed topological anchors of the matrix in the fibre [21,31,51]. The thermal shock strongly decreased the stress transmit capacity of ΔT -PAN composites that achieved the maximum stiffness at $D_F = 46\%$ ($\mu\varepsilon = 1501 \mu\text{m/m}$), while ΔT -PITCH composites did not show a significant increase of D_F to saturate the load transmission ($D_F = 20\%$ and $\mu\varepsilon = 765 \mu\text{m/m}$). In both cases, the stress achieved at the end of this stage increased after thermal shock. Recently Li [52] reported how the stress transfer capacity between the fibre and the matrix is inversely proportional to the debonding fraction at the interface of an unidirectional T-700™ C/SiC composite. In agreement with this conclusion, it is reasonable that thermal shock increased the fraction of debonded matrix/fibre interface, or more in general decreased stress transmit capacity between the fibre and the matrix of the AP-PAN composite.

3.3.3 Load-bearing fibres stage

After the “matrix-fibre stress transmission” stage, AP-PAN composites become constant up to the onset of failure at $\sigma_1 = 264 \text{ MPa}$, $D_F = 89\%$ and $\mu\varepsilon = 2919 \mu\text{m/m}$. This constant elastic behaviour was observed after thermal shock as well, although the failure onset occurred earlier at 219 MPa, $D_F = 87\%$ and $\mu\varepsilon = 2829 \mu\text{m/m}$. This linearity was ascribed to the linear elastic behaviour of the load-bearing fibre [53] and the absence of significant failure events. The lower extension of the “load-bearing fibres” stage of ΔT -PAN, with respect to AP-PAN composites (1338 $\mu\text{m/m}$ vs 1826 $\mu\text{m/m}$), and their early failure onset agree with the matrix/fibre debonding induced by thermal shock. In other words, interfaces debonding first prevented saturation of the stiffness and then promoted interlaminar crack growth at a lower critical stress (219 MPa vs 264 MPa).

Unlike the AP-PAN composites, the curve of the AP-PITCH composites did not show plateau. The stiffness decreasing of AP-PITCH composites should be ascribed to the matrix-cracking phenomena and the consequent elongation of the specimen along the

longitudinal direction due to the spring-back of the inner freed fibres (IFF) that released their residual compression strain [20]. In fact, the releasing of the compressive strain should lead to an increment of the displacement although the increment of the applied load is equal to zero. It can be seen that matrix-cracking stage covered all the stiff degradation up to its relative minimum. This means that in this stage the crack density increased until reaching the saturation level of the crack density. After the matrix-cracking stage, the relaxed parts of fibres (those above called IFF) were gradually taut and straightened leading to a recovery of 97 ± 11 % of the maximum stiffness measured before the matrix-cracking onset.

The cause of this stiffness recovery after matrix-cracking is still unclear and many hypotheses were put forward:

- (i) a better alignment of the IFFs compensated the loss of matrix stiffness;
- (ii) the overall stiffness was determined by stiffness of composite blocks hypothesizing that they were in series with IFFs and their fraction did not significantly change even at the saturation of matrix cracking [54];
- (iii) RTSs reduced the equivalent stiffness of the composite and their release compensated the matrix damage [21];
- (iv) Braess paradox [55]: the high modulus of the UHTC phase (about 420 GPa [56]), fibre waviness and misalignment with respect to the applied stress and the strong interlocked matrix/fiber interfaces resulted in matrix forming “cross-links” between neighbour fibres and making them work in series rather than in parallel. When releasing of RTSs occurred (i.e. the cross-links were cut), the stresses distribution made more fibres work in parallel and compensated the matrix damage.

Interestingly, after thermal shock treatments, all this continuous change in stiffness disappeared leaving a plateau. This observation suggests that thermal shock had previously induced matrix-cracking rather than fibre/matrix debonding since no stiffness decrease was observed in the load-bearing fibre stage, i.e. no significant formation of IFF occurred during bending tests of the ΔT -PITCH composites. Moreover, this observation is in agreement with the finding that the transition between “matrix-fibre stress transmission” to “load-bearing fibres” stage of ΔT -PITCH composites ($D_F = 20\%$ and $\mu_\varepsilon = 765 \mu\text{m/m}$) was comparable with respect to that of AP-PITCH composites ($D_F = 17\%$ and $\mu_\varepsilon = 592 \mu\text{m/m}$), i.e. no matrix/fibre debonding hamstrung the load transmission. On the other hand, the missing of an extended matrix-cracking stage and formation of IFF, during the bending

test, increased the stress rate and brought to reach the critical stress of failure onset (about 200 MPa for both the AP- and Δ T-PITCH composites) at $D_F = 57\%$ and $\mu\varepsilon = 1756\ \mu\text{m/m}$ instead of 73 % and 2829 $\mu\text{m/m}$.

This evidence suggests that RTSs gave to the material a “plasticity reserve” that shift the failure onset. Similar observations about the effect of thermal shock on the releasing of RTSs was also observed through Vickers imprints on similar composites [20]. In this previous work it was observed that imprints on as-produced composites resulted in material pileup onto the fibres’ plane or the appearance of out-of-plane freed fibres (OFF) as consequence of matrix-cracking and spring-back of the compressed fibres (i.e. releasing of their residual compression strain). After thermal shock, the imprints showed a higher elastic recovery (in other words the thermally shocked composites showed the tendency to close the imprint along the direction of the fibre axis) due to the large amount of IFF previously produced by the thermal treatment.

3.3.4 Failure stage

As for AP-PAN material, the decrease of stiffness after the failure onset was mainly ascribed to interlaminar crack propagation. In fact, the “apparent” flexural strength of 298 ± 54 MPa, obtained with a span-to-thickness ratio (s/t) of 5, was increased up to 631 ± 12 MPa by increasing s/t up to 20 [40]. The significant increase of the maximum flexural stress with the increasing of s/t confirms that the failure of small beams (s/t= 5) was dominated by shear stress (mode II) [41]. —It is worth noting that the high strength value obtained with s/t of 20 well match that of composites produced by Airbus (former EADS) that have the same type and amount of fibre— The mode II dominated behaviour of PAN composites was triggered by the lower matrix densification (ρ_m), lower fibre infiltration (ρ_b) and dispersion (B). Hence, according to the classical beam theory ($\tau = \frac{\text{thickness}}{\text{lower span}} \sigma = \frac{2}{20} \sigma$), the onset and the critical interlaminar shear stress of PAN composites were attested at 26 ± 5 MPa and 30 ± 5 MPa, respectively. These values decreased down to 22 ± 1 MPa and 25 ± 3 MPa after thermal shock as a consequence of the increased debonding fraction at the interface. In case of AP-PITCH composites, the mode II contribution was limited due to the higher strength of both the matrix and the interfaces. The “apparent” flexural strength of 255 ± 24 MPa, obtained with s/t = 5, was increased up to 329 ± 9 MPa by increasing s/t up to 20. This increment of about 30% is quite lower than that of AP-PAN composites, which was more than 200%, and suggests a lower contribution of

mode II in the failure of AP-PITCH sample. The raised ultimate strength of Δ T-PITCH specimens should be attributed to the releasing of RTSs through matrix-cracking and to the absence of an evident increase of the fraction of the debonded matrix/fibre interface. In fact, according to Evans and Marshall [57], the delamination growing is strongly favoured by RTSs while appears unlikely if RTSs are released and, according to and Liao and Reifsnider [58], the fibre failure is favoured in the debonded region rather than at the matrix crack plane or at the bonded region, respectively. Hence, it is reasonable that the released RTSs through matrix-cracking reduced the probability of fibre/matrix debonding under shear stress in Δ T-PITCH specimens during the bending test. This results in a fibre failure probability shifted towards higher flexural stress values due to the hindered formation of debonded regions. It is worth noting that the failure onset should be considered as the fibre failure onset. In fact, the failure onset stress was not changed by thermal shock. Finally, according with the fibre failure models [58,59], as fibres begin to break, the loads is redistributed to the intact fibres gradually leading to the decrease of the stiffness that was observed before the failure.

3.4 Flexural strength at high temperature

In this paragraph we compared the RT flexural strength values of AP- and Δ T-composites with those obtained at 1500°C of AP-composites. Unlike thermal shock, the bending test at high temperature has the advantage to release the thermal stress—in principle—without inducing damage. This comparison allows to further assess the level of RTSs on the PAN and PITCH composites.

As showed in Fig.7, the flexural strength of Δ T-PITCH composites increased by 38%, while $\sigma_1^{\Delta T}$ of Δ T-PAN composites showed a decrement of 16%. This evidence supports that the benefit of RTSs releasing was hidden by the thermal damage only in the latter case. Another proof of the larger amount of RTSs in AP-PITCH composites is given by the larger increase (+73% instead of +23%) of flexural strength observed at 1500 °C. Unlike the bending tests of thermally shocked specimens, the bending tests at high temperature of the as-produced specimens are not strongly affected by thermal damages. In case of the bending tests at high temperature, the changes with respect to the bending tests at RT should be mainly attributed to the release of the RTSs. In a previous work [23], where it was possible to collect the load-displacement curve during tensile and bending test at high temperature up to 1800 °C for a composite similar to the PITCH one, the loss of the above described trends as the curve lost the characteristic three-stage deformation (three stages

if the “fixture-specimen alignment stage” is excluded) was observed. In particular, the lowering of the stiffness followed by an its increase in the "load-bearing fibres" stage was absent, which is present in the RT tests a consequence of IFFs formation and their subsequent loading.

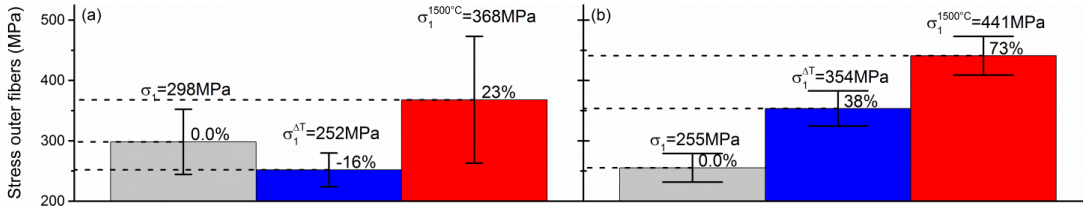


Fig.7 Flexural strength values at room temperatures and 1500 °C (σ_1 and $\sigma_1^{1500^\circ\text{C}}$, respectively) of as produced (a) PAN and (b) PITCH composites and after thermal shock ($\sigma_1^{\Delta T}$).

3.5 Cycled dilatometry

The effect of RTSS on thermal stability of AP-composites was investigated through the cycled dilatometry in terms of residual permanent deformation ($\Delta L_i/L_0$) and coefficient of thermal expansion (CTE) variations. Moreover, the CTE analysis allowed to probe the changes of the overall modulus of the matrix by applying the Schapery's model [21]. All extrapolated data from cycled dilatometry are reported in appendix C together with the coefficients of the polynomials that match the trend of CTE within the entire investigated temperature range. Cycled dilatometry showed an evident evolution of $\Delta L_i/L_0$ and CTE in AP-PITCH composites (Fig.8). The positive increase of $\Delta L_i/L_0$ as function of thermal cycles is consisted with the matrix-cracking and the release of the compressive strain of fibre. Once new inner freed fibres (IFF) are formed, the specimen elongated and showed a lower CTE as consequence of the higher discontinuity produced in the matrix. The curvature fitting with Schapery's model revealed that Young's modulus of the matrix steady decreased from about 157 GPa to 126 GPa with thermal cycles (inset of Fig.8). This trend reaffirms that RTSS are present in the AP-PITCH composites and led to matrix cracking during thermal cycles. However, thermal damaging experienced by AP-PITCH composite is quite lower than that observed with the same method in UHTCMC consolidated by reactive sintering [21]. In this latter case, CTE decreased of 52 % instead of 11 %, a permanent expansion of 0.47 % instead of 0.03% was measured, and the matrix modulus, instead of decreasing by 20%, dropped by 90% [21]. On the other hand, AP-PAN composites, owing to the lower level of RTSS, guaranteed by the PyC coating and the

lower matrix densification, showed a higher thermomechanical stability. In fact, a negligible variation of $\Delta L_i/L_0$ and CTE was observed (inset of Fig.8).

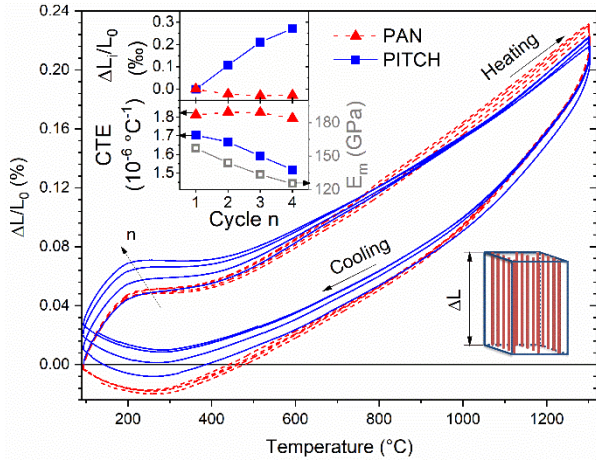


Fig.8 Four consecutive cycles (n) of dilatometry (also called thermomechanical analysis, TMA) plotted as relative dimensional change ($\Delta L/L_0$) vs. temperature of as-produced PAN (red dashed line) and PITCH (blue solid line) unidirectional composites along the longitudinal direction. The inset graphs show the residual permanent deformation ($\Delta L_i/L_0$) in ‰, the coefficient of thermal expansion (CTE) and the Young's modulus of the matrix (E_m) as function of thermal cycle (n) for PAN (triangle symbol) and PITCH (square symbol) composites.

3.6 Comparison between highly and low stresses composites

In a previous work, properties and microstructures of UHTCMCs with PAN- or pitch-derived fibres were qualitatively compared [31]. The deeper analysis conducted in this work allows to make a step further in the comprehension of the thermo-mechanical behaviour in relationship with the stress state, in turn related to compositions and process.

The obtained results suggest that for UHTCMCs consolidated through sintering techniques there is a trade-off between, on one hand, transverse strength, oxidation and ablation resistance and, on the other hand, thermal dimensional stability. In fact, if the matrix densification improves transversal properties [20,31], the oxidation [16] and ablation resistance [31], on the other side, enhances the RTSs compromising the thermal stability. From the technological point of view, the forfeited strain could play a positive role in RT applications by shifting the fibre failure onset to higher applied deformation. Moreover, the residual stress release by the matrix-cracking is a minor concern, since these highly stressed UHTCMCs are intrinsically 'damage-tolerant' and 'notch-insensitive'—even along the transverse direction [20]—show an increase of strength after thermal shock, and can be shocked at temperatures higher than 1500 °C [20,48]. On the other hand, the lower

thermal stability of highly stressed UHTCMCs suggests that further studies are required to (i) assess the effect of mild annealing treatments (such as thermal cycles that can be design as “workout” or “break-in” steps to release the residual strain) on the structural and environmental properties. (ii) It is of interest to understand if the formation of IFFs can be exploited (e.g. the formation of IFFs may guarantee a better performance of composite joints, such as interference-fit joints, under extreme temperatures, and may contrast the nozzle throat erosion and keep constant the nozzle throat area for more time), or it is strictly needed "design against RTSs" to improve the long-term durability of UHTCMCs components that are subjected to thermal cycles at high temperatures. In any case, for a safe and reliable design against thermomechanical fatigue, the formation of IFFs cannot be neglected, but should be considered in suitable models for the quantitative assessment of the thermomechanical behaviour.

4 Conclusion

Composites with tailored levels of residual thermal stresses (RTSs) were produced. It was observed that PyC coating not only guaranteed a weak fibre/matrix interphase but also led to a lower degree of fibre distribution into the matrix and to a higher matrix porosity. These features lowered the matrix-fibre interactions and consequently the residual stress accumulated during the cooling phase of the consolidation process. On the contrary, uncoated ultra-high modulus pitch-derived fibres allowed to obtain well dispersed and anchored fibres to dense matrix resulting in high level of RTSs. The thermomechanical investigation showed that:

- (1) elastic moduli of the low stressed composite agree with the classical laminate theory. On the contrary a discrepancy between the measured moduli and the theoretical ones was found in case of highly stressed composite.
- (2) RTSs affected the stress-strain response and thermal stability. On one side, RTSs gave a plasticity reserve and shifted the failure onset toward higher strain values. On the other side RTSs lowered the strength at RT and made the component of UHTCMC prone to permanent deformations during thermal cycles. As for slightly stressed composites produced with PyC-coated fibres, the higher thermal stability was obtained at the expense of transversal strength and interlaminar shear strength.

More work is needed for further understanding other non-intuitive experimental findings about:

- (1) the effect of the different porosities (i.e. matrix porosity, inter fibre porosity and porosity between fibre and coating) on the mechanical behaviour.
- (2) The stiffness response of highly stressed composites and in particular its recovery after matrix-cracking and the formation of inner freed fibres.
- (3) The mechanical behaviour of highly stressed composites after repeated thermal cycles (e.g. how does the stress/strain to failure and the elastic moduli change?).
- (4) The use of thermomechanical tests to extrapolate proxy data on the residual stresses.

Acknowledgements

This work received support by the European Union's Horizon 2020 research and innovation programme under Grant Agreement n° 685594. (C³HARME: Next Generation Ceramic Composites for Harsh Combustion Environment and Space). Authors wish to acknowledge P. Mittermeier (AIRBUS), F. Meistring (ARIANEGROUP) for supplying coated PAN-derived C fibres and technical support in the filament winding procedure, S. Rivera (Nanoker Research S.L.) for SPS cycles.

References

- [1] Drenthe NT, Zandbergen BTC, Curran R, Van Pelt MO. Cost estimating of commercial smallsat launch vehicles. *Acta Astronaut* 2019;155:160–9. <https://doi.org/10.1016/J.ACTAASTRO.2018.11.054>.
- [2] Li WJ, Cheng DY, Liu XG, Wang YB, Shi WH, Tang ZX, et al. On-orbit service (OOS) of spacecraft: A review of engineering developments. *Prog Aerosp Sci* 2019;108:32–120. <https://doi.org/10.1016/j.paerosci.2019.01.004>.
- [3] Padture NP. Advanced structural ceramics in aerospace propulsion. *Nat Mater* 2016;15:804–9. <https://doi.org/10.1038/nmat4687>.
- [4] Hald H. Operational limits for reusable space transportation systems due to physical boundaries of C/SiC materials. *Aerosp Sci Technol* 2003;7:551–9. [https://doi.org/10.1016/S1270-9638\(03\)00054-3](https://doi.org/10.1016/S1270-9638(03)00054-3).
- [5] Wang X, Wei K, Tao Y, Yang X, Zhou H, He R, et al. Thermal protection system integrating graded insulation materials and multilayer ceramic matrix composite cellular sandwich panels. *Compos Struct* 2019;209:523–34. <https://doi.org/10.1016/J.COMPSTRUCT.2018.11.004>.
- [6] Rubio V, Binner J, Cousinet S, Le Page G, Ackerman T, Hussain A, et al. Materials

characterisation and mechanical properties of Cf-UHTC powder composites. *J Eur Ceram Soc* 2019;39:813–24.

<https://doi.org/10.1016/J.JEURCERAMSOC.2018.12.043>.

- [7] Zhang D, Hu P, Dong S, Liu X, Wang C, Zhang Z, et al. Oxidation behavior and ablation mechanism of Cf/ZrB₂-SiC composite fabricated by vibration-assisted slurry impregnation combined with low-temperature hot pressing. *Corros Sci* 2019;161. <https://doi.org/10.1016/j.corsci.2019.108181>.
- [8] Ouyang H, Zhang Y, Li C, Li G, Huang J, Li H. Effects of ZrC/SiC ratios on mechanical and ablation behavior of C/C–ZrC–SiC composites prepared by carbothermal reaction of hydrothermal co-deposited oxides. *Corros Sci* 2019;163:108239. <https://doi.org/10.1016/j.corsci.2019.108239>.
- [9] Rueschhoff LM, Carney CM, Apostolov ZD, Cinibulk MK. Processing of fiber-reinforced ultra-high temperature ceramic composites: A review. *Int J Ceram Eng Sci* 2020;2:22–37. <https://doi.org/10.1002/ces2.10033>.
- [10] Tatarko P, Valenza F, Ünsal H, Kovalčíková A, Sedláček J, Šajgalík P. Design of Lu₂O₃-reinforced Cf/SiC-ZrB₂-ZrC Ultra-High Temperature Ceramic Matrix Composites: Wetting and interfacial reactivity by ZrSi₂ based alloys. *J Eur Ceram Soc* 2020. <https://doi.org/10.1016/j.jeurceramsoc.2020.05.055>.
- [11] Zhang D, Feng J, Hu P, Xun L, Liu M, Dong S, et al. Enhanced mechanical properties and thermal shock resistance of Cf/ZrB₂-SiC composite via an efficient slurry injection combined with vibration-assisted vacuum infiltration. *J Eur Ceram Soc* 2020. <https://doi.org/10.1016/j.jeurceramsoc.2020.07.003>.
- [12] Ni D, Cheng Y, Zhang J, Liu J-X, Zou J, Chen B, et al. Advances in ultra-high temperature ceramics, composites, and coatings. *J Adv Ceram* 2021 111 2021;11:1–56. <https://doi.org/10.1007/S40145-021-0550-6>.
- [13] Zhang X, Chen Y, Hu J. Recent advances in the development of aerospace materials. *Prog Aerosp Sci* 2018;97:22–34. <https://doi.org/10.1016/j.paerosci.2018.01.001>.
- [14] Rajak DK, Pagar DD, Kumar R, Pruncu CI. Recent progress of reinforcement materials: A comprehensive overview of composite materials. *J Mater Res Technol* 2019;8:6354–74. <https://doi.org/10.1016/j.jmrt.2019.09.068>.
- [15] Sciti D, Zoli L, Silvestroni L, Cecere A, Di Martino GD, Savino R. Design, fabrication and high velocity oxy-fuel torch tests of a Cf-ZrB₂ - fiber nozzle to evaluate its potential in rocket motors. *Mater Des* 2016;109:709–17.

<https://doi.org/10.1016/j.matdes.2016.07.090>.

- [16] Galizia P, Vinci A, Zoli L, Monteverde F, Binner J, Venkatachalam V, et al. Retained strength of UHTCMCs after oxidation at 2278 K. *Compos Part A Appl Sci Manuf* 2021;149:106523. <https://doi.org/10.1016/j.compositesa.2021.106523>.
- [17] Venkatachalam V, Blem S, Gülhan A, Binner J. Thermal Qualification of the UHTCMCs Produced Using RF-CVI Technique with VMK Facility at DLR. *J Compos Sci* 2022, Vol 6, Page 24 2022;6:24. <https://doi.org/10.3390/JCS6010024>.
- [18] Galizia P, Failla S, Zoli L, Sciti D. Tough salami-inspired Cf/ZrB₂ UHTCMCs produced by electrophoretic deposition. *J Eur Ceram Soc* 2018;38:403–9. <https://doi.org/10.1016/j.jeurceramsoc.2017.09.047>.
- [19] Zoli L, Vinci A, Galizia P, Gutiérrez-Gonzalez CF, Rivera S, Sciti D. Is spark plasma sintering suitable for the densification of continuous carbon fibre - UHTCMCs? *J Eur Ceram Soc* 2020;40:2597–603. <https://doi.org/10.1016/j.jeurceramsoc.2019.12.004>.
- [20] Galizia P, Sciti D, Saraga F, Zoli L. Off-axis damage tolerance of fiber-reinforced composites for aerospace systems. *J Eur Ceram Soc* 2020;40:2691–8. <https://doi.org/10.1016/j.jeurceramsoc.2019.12.038>.
- [21] Galizia P, Zoli L, Sciti D. Impact of residual stress on thermal damage accumulation, and Young's modulus of fiber-reinforced ultra-high temperature ceramics. *Mater Des* 2018;160:803–9. <https://doi.org/10.1016/J.MATDES.2018.10.019>.
- [22] Pradere C, Sauder C. Transverse and longitudinal coefficient of thermal expansion of carbon fibers at high temperatures (300–2500 K). *Carbon N Y* 2008;46:1874–84. <https://doi.org/10.1016/j.carbon.2008.07.035>.
- [23] Sciti D, Zoli L, Reimer T, Vinci A, Galizia P. A systematic approach for horizontal and vertical scale up of sintered Ultra-High Temperature Ceramic Matrix Composites for Aerospace – Advances and perspectives. *Compos Part B* 2022.
- [24] Koch D. Microstructural Modeling and Thermomechanical Properties. *Ceram. Matrix Compos.*, Weinheim, Germany: Wiley-VCH Verlag GmbH & Co. KGaA; n.d., p. 231–59. <https://doi.org/10.1002/9783527622412.ch10>.
- [25] Tu W-C, Lange FF, Evans AG. Concept for a Damage-Tolerant Ceramic Composite with “Strong” Interfaces. *J Am Ceram Soc* 1996;79:417–24. <https://doi.org/10.1111/j.1151-2916.1996.tb08138.x>.
- [26] Carelli EA V., Fujita H, Yang JY, Zok FW. Effects of Thermal Aging on the Mechanical Properties of a Porous-Matrix Ceramic Composite. *J Am Ceram Soc* 2004;85:595–602. <https://doi.org/10.1111/j.1151-2916.2002.tb00138.x>.

- [27] Yan N, Fu Q, Zhang S, Zhang J, Sun J, Shen Q. Effects of thermal shock on the microstructure, mechanical and thermophysical properties of ZrC-C composites. *Compos Part A Appl Sci Manuf* 2021;151:106642. <https://doi.org/10.1016/J.COMPOSITESA.2021.106642>.
- [28] HU J, ZHANG K, CHENG H, ZOU P. Modeling on mechanical behavior and damage evolution of single-lap bolted composite interference-fit joints under thermal effects. *Chinese J Aeronaut* 2021;34:230–44. <https://doi.org/10.1016/J.CJA.2020.09.023>.
- [29] Mei H, Bai Q, Sun Y, Li H, Wang H, Cheng L. The effect of heat treatment on the strength and toughness of carbon fiber/silicon carbide composites with different pyrolytic carbon interphase thicknesses. *Carbon N Y* 1970;57:288–97. <https://doi.org/10.1016/j.carbon.2013.01.076>.
- [30] Zhang D, Hu P, Dong S, Qu Q, Zhang X. Effect of pyrolytic carbon coating on the microstructure and fracture behavior of the Cf/ZrB₂-SiC composite. *Ceram Int* 2018;44:19612–8. <https://doi.org/10.1016/J.CERAMINT.2018.07.210>.
- [31] Sciti D, Zoli L, Vinci A, Silvestroni L, Mungiguerra S, Galizia P. Effect of PAN-based and pitch-based carbon fibres on microstructure and properties of continuous Cf/ZrB₂-SiC UHTCMCs. *J Eur Ceram Soc* 2020;41:3045–50. <https://doi.org/10.1016/j.jeurceramsoc.2020.05.032>.
- [32] Wang Z, Fang G, Wang B, Hu P, Yi F, Meng S. Study on toughening mechanisms of pyrolytic carbon interface layer in Cf/ZrB₂-SiC composites using in-situ tensile experimental and numerical methods. *J Eur Ceram Soc* 2021. <https://doi.org/10.1016/j.jeurceramsoc.2021.04.028>.
- [33] Cheng T. Understanding the ultra-high-temperature mechanical behaviors of advanced two-dimensional carbon-carbon composites. *Ceram Int* 2020. <https://doi.org/10.1016/j.ceramint.2020.05.237>.
- [34] Sha J, Wang S, Dai J, Zu Y, Li W, Sha R. High-temperature Mechanical Properties and Their Influence Mechanisms of ZrC-Modified C-SiC Ceramic Matrix Composites up to 1600 °C. *Materials (Basel)* 2020;13:1581. <https://doi.org/10.3390/ma13071581>.
- [35] Longbiao L. Damage evolution of fiber-reinforced ceramic-matrix composites under stress-rupture and cyclic loading at elevated temperature in oxidizing atmosphere. *Int J Mech Sci* 2017;131132:938–55. <https://doi.org/10.1016/j.ijmecsci.2017.08.009>.
- [36] Longbiao L. Damage and failure of fiber-reinforced ceramic-matrix composites subjected to cyclic fatigue, dwell fatigue and thermomechanical fatigue. *Ceram Int* 2017;43:13978–96. <https://doi.org/10.1016/j.ceramint.2017.07.130>.

- [37] Longbiao L. Time-dependent damage and fracture of fiber-reinforced ceramic-matrix composites at elevated temperatures. *Compos Interfaces* 2019;26:963–88. <https://doi.org/10.1080/09276440.2019.1569397>.
- [38] GUO J, FU H, PAN B, KANG R. Recent progress of residual stress measurement methods: A review. *Chinese J Aeronaut* 2021;34:54–78. <https://doi.org/10.1016/J.CJA.2019.10.010>.
- [39] Chen BW, Ni DW, Liao CJ, Jiang YL, Lu J, Ding YS, et al. Chemical reactions and thermal stress induced microstructure evolution in 2D-Cf/ZrB₂-SiC composites. *J Mater Sci Technol* 2021;83:75–82. <https://doi.org/10.1016/J.JMST.2020.12.054>.
- [40] Sciti D, Galizia P, Reimer T, Schoberth A, Gutiérrez-Gonzalez CF, Silvestroni L, et al. Properties of large scale ultra-high temperature ceramic matrix composites made by filament winding and spark plasma sintering. *Compos Part B Eng* 2021. <https://doi.org/10.1016/j.compositesb.2021.108839>.
- [41] Galizia P, Sciti D, Jain N. Insight into microstructure and flexural strength of ultra-high temperature ceramics enriched SICARBON™ composite. *Mater Des* 2021;109888. <https://doi.org/10.1016/j.matdes.2021.109888>.
- [42] Sepahvand KK. Deep Learning Based Uncertainty Analysis in Computational Micromechanics of Composite Materials. *Appl Mech* 2021, Vol 2, Pages 559-570 2021;2:559–70. <https://doi.org/10.3390/APPLMECH2030031>.
- [43] Mishurova T, Rachmatulin N, Fontana P, Oesch T, Bruno G, Radi E, et al. Evaluation of the probability density of inhomogeneous fiber orientations by computed tomography and its application to the calculation of the effective properties of a fiber-reinforced composite. *Int J Eng Sci* 2018;122:14–29. <https://doi.org/10.1016/J.IJENGSCI.2017.10.002>.
- [44] Requena G, Fiedler G, Seiser B, Degischer P, Di Michiel M, Buslaps T. 3D-Quantification of the distribution of continuous fibres in unidirectionally reinforced composites. *Compos Part A Appl Sci Manuf* 2009;40:152–63. <https://doi.org/10.1016/J.COMPOSITESA.2008.10.014>.
- [45] Sepahvand K, Marburg S. On Construction of Uncertain Material Parameter using Generalized Polynomial Chaos Expansion from Experimental Data. *Procedia IUTAM* 2013;6:4–17. <https://doi.org/10.1016/J.PIUTAM.2013.01.001>.
- [46] Sause MGR. Failure of fiber-reinforced composites. *Springer Ser. Mater. Sci.*, vol. 242, Springer Verlag; 2016, p. 5–55. https://doi.org/10.1007/978-3-319-30954-5_2.
- [47] de Pablo JJ, Jackson NE, Webb MA, Chen LQ, Moore JE, Morgan D, et al. New

frontiers for the materials genome initiative. *Npj Comput Mater* 2019;5:1–23.
<https://doi.org/10.1038/s41524-019-0173-4>.

- [48] Zoli L, Vinci A, Galizia P, Melandri C, Sciti D. On the thermal shock resistance and mechanical properties of novel unidirectional UHTCMCs for extreme environments. *Sci Rep* 2018;8:9148. <https://doi.org/10.1038/s41598-018-27328-x>.
- [49] Uhlmann F, Wilhelmi C, Schmidt-Wimmer S, Beyer S, Badini C, Padovano E. Preparation and characterization of ZrB₂ and TaC containing Cf/SiC composites via Polymer-Infiltration-Pyrolysis process. *J Eur Ceram Soc* 2017;37:1955–60.
<https://doi.org/10.1016/j.jeurceramsoc.2016.12.048>.
- [50] Servadei F, Zoli L, Galizia P, Vinci A, Sciti D. Development of UHTCMCs via water based ZrB₂ powder slurry infiltration and polymer infiltration and pyrolysis. *J Eur Ceram Soc* 2020. <https://doi.org/10.1016/j.jeurceramsoc.2020.05.054>.
- [51] Greenfeld I, Rodricks CW, Sui XM, Wagner HD. Beaded fiber composites—Stiffness and strength modeling. *J Mech Phys Solids* 2019;125:384–400.
<https://doi.org/10.1016/j.jmps.2018.12.020>.
- [52] Li L. Effect of temperature on matrix multicracking evolution of C/SiC fiber-reinforced ceramic-matrix composites. *High Temp Mater Process* 2020;39:189–99.
<https://doi.org/10.1515/htmp-2020-0044>.
- [53] Sauder C, Lamon J, Pailier R. The tensile behavior of carbon fibers at high temperatures up to 2400 °C. *Carbon N Y* 2004;42:715–25.
<https://doi.org/10.1016/j.carbon.2003.11.020>.
- [54] Galizia P, Reimer T, Binner J, Venkatachalam V, Lagos MA, Zoli L, et al. Characterization of different ultra-high temperature ceramic matrix composites on elastic modulus and tensile and flexural strength up to 1800 ° C. *Compos Part A* 2021;Under Revi.
- [55] Penchina CM, Penchina LJ. The Braess paradox in mechanical, traffic, and other networks. *Am J Phys* 2003;71:479. <https://doi.org/10.1119/1.1538553>.
- [56] Monteverde F, Guicciardi S, Bellosi A. Advances in microstructure and mechanical properties of zirconium diboride based ceramics. *Mater Sci Eng A* 2003;346:310–9.
[https://doi.org/10.1016/S0921-5093\(02\)00520-8](https://doi.org/10.1016/S0921-5093(02)00520-8).
- [57] EVANS AG, MARSHALL DB. The Mechanical Behavior of Ceramic Matrix Composites. *Proc. 7th Int. Conf. Fract.*, Elsevier; 1989, p. 3593–641.
<https://doi.org/10.1016/b978-0-08-034341-9.50251-5>.
- [58] Liao K, Reifsnider KL. A tensile strength model for unidirectional fiber-reinforced

brittle matrix composite. *Int J Fract* 2000 106:2000;106:95–115.

<https://doi.org/10.1023/A:1007645817753>.

- [59] Li LB, Song YD, Sun YC. Modeling the tensile behavior of unidirectional C/SiC ceramic-matrix composites. *Mech Compos Mater* 2014;49:659–72.
<https://doi.org/10.1007/S11029-013-9382-Y>.
- [60] Walpole LJ. On bounds for the overall elastic moduli of inhomogeneous systems—II. *J Mech Phys Solids* 1966;14:289–301.
- [61] Rice RW. Evaluation and extension of physical property-porosity models based on minimum solid area. *J Mater Sci* 1996;31:102–118.
<https://doi.org/10.1007/BF00355133>.
- [62] Harris B, Institute of Materials (London E. Engineering composite materials. London: IOM; 1999.

Appendix A

For dissemination purpose and facilitation of discovery, modelling and design of developed materials, the parameters of fitted Cumulative Distribution Functions (CDFs) of the analysed microstructural “material genome” [47] are shown in Table A.1. Further microstructural and mechanical analyses were presented in previous works [19,31,40]. In particular, further data of PAN sample were published in the Ref.s [19], [31] and [40] under the following labels: “C_SPS”, “PAN” and “AIR-M”, respectively. Data of PITCH sample were published in the Ref.s [19] and [31] under the following labels: “U_SPS” and “PITCH”, respectively.

Table A.1. Parameters of fitted CDFs according to Eq. (1) and (2) and experimental data showed in Fig.s (3,4). Where D , T , p_i , B , p_b , θ , p_m and S is fibre diameter, thickness of fibre coating, size of cavities between fibre and coating, area of fibres bundle (B), size of intrabundle voids, size of matrix pores, fibre misalignment and cracks spacing, respectively.

PAN										
x	Eq.	p_1	x_1	a_1	b_1	$FWHM_1$	x_2	a_2	b_2	$FWHM_2$
D (μm)	(1)	1	5.04676	0.13694	1	0.5	0	1	0	-
T (μm)	(1)	1	0.64123	0.06295	1	0.3	0	1	0	-
p_i (μm)	(1)	0.43527	1.17276	-0.33379	0	1.4	0.40275	-0.09429	-1	0.3
B (μm^2)	(2)	-	30.15242	1.80573	0.23776	44	-	-	-	-
p_b (μm)	(2)	-	2.87942	3.21701	1.03242	2.6	-	-	-	-
θ ($^\circ$)	(1)	0.44925	0.46175	-0.58744	0	2.0	2.38232	-1.46076	-1	5.5

PITCH										
D (μm)	(1)	0.69578	9.66662	-0.47642	0	1.8	11.17663	-0.41936	-1	1.4
B (μm^2)	(2)	-	44.051	2.61768	0.13024	50	-	-	-	-
p_b (μm)	(2)	-	4.72281	2.63498	0	6.4	-	-	-	-
θ ($^\circ$)	(1)	0.40189	-1.32425	-0.84522	0	3.1	4.02646	-1.30525	-1	4.8
p_m (μm)	(2)	-	0.35927	1.80222	0	0.6	-	-	-	-
S (μm)	(1)	1	22.28647	10.22215	1.08099	36	0	1	0	-

Appendix B

The elastic properties of the composites of Table B.1 were calculated starting from the elastic properties of single phases and their amount. The elastic properties of the matrices were estimated via the Walpole model [60] and the exponential law [61]. In case of PITCH composite the high value of 13 for the numerical constant b accounts for matrix-cracks patterns. It is worth noting that Walpole model gave a larger range of values for PAN

composite due to the presence of PyC that was considered as a matrix phase. The elastic moduli of the single plies were calculated by using simple micromechanics models, i.e. rule of mixtures and inverse rule of mixtures [62]. Finally, the elastic moduli of the unidirectional composites were estimated by considering the orientation dependence of the fibre reinforcement by integrating the observed distribution of the angle fibre misalignment into the classical laminate theory [41].

Table B.1. Microstructural and elastic properties values of the single phases, matrix, unidirectional lamina and unidirectional 0/0° composite.

Elastic property	Symbol	Unit	PAN			PITCH
SINGLE PHASES						
Fibre volumetric content	V_f	%	34			51
Longitudinal modulus of the fibre	$E_{f,1}$	GPa	294			780
Transverse modulus of the fibre	$E_{f,2}$	GPa	15			10
In-plane shear modulus of the fibre	$G_{f,12}$	GPa	10			5
Major Poisson's ratio of the fibre	$\nu_{f,12}$		0.25			0.25
Young's modulus of PyC	E_{PyC}	GPa	20			-
Shear modulus of PyC	G_{PyC}	GPa	5			-
Young's modulus of SiC	E_{SiC}	GPa	410			410
Shear modulus of SiC	G_{SiC}	GPa	180			180
Young's modulus of UHTC	E_{UHTC}	GPa	540			540
Shear modulus of UHTC	G_{UHTC}	GPa	210			210
MATRIX						
Exponential constant related to porosity	b		4			13
Overall porosity	p	%	18			8
Young's modulus of the matrix	E_m	GPa	22	-	98	157
Shear modulus of the matrix	G_m	GPa	8	-	38	61
Poisson's ratio of the matrix	ν_m		0.3			0.3
COMPOSITE PLY						
Longitudinal modulus of a composite ply	$E_{ply,1}$	GPa	114	-	165	475
Transverse modulus of a composite ply	$E_{ply,2}$	GPa	19	-	34	18
Shear modulus of a composite ply	$G_{ply,12}$	GPa	9	-	19	9
Major Poisson's ratio of a composite ply	$\nu_{ply,12}$		0.28			0.27
COMPOSITE						
Longitudinal modulus of the 0/0° composite	$E_{c,1}$	GPa	112	-	163	399
Transverse modulus of the 0/0° composite	$E_{c,2}$	GPa	19	-	34	19
Shear modulus of the 0/0° composite	$G_{c,12}$	GPa	9	-	19	9

Appendix C

For the same reasons claimed in the appendix A, the simplified stress-strain curves and the corresponding representative values are showed in Fig. C.1 and Table C.1, respectively.

The characteristic points of the dilatometric curves, the secant coefficients of thermal expansion, the fitting parameters of the coefficient of thermal expansion curves and the Young's modulus of the matrix for each thermal cycle are reported in Table C.2.

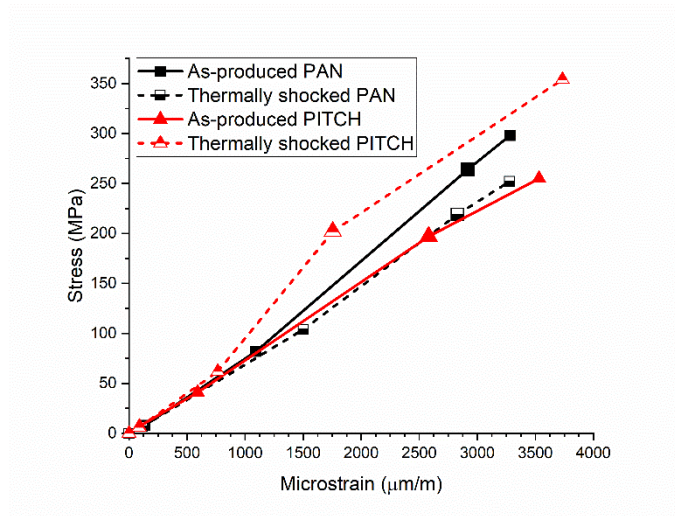


Fig. C.1. Simplified flexural stress-strain curves of as-produced (solid lines and symbols) and thermally shocked (dashed lines and half symbols) PAN (black squares) and PITCH (red triangles) samples. For each curve the stress-strain points mark the transition from "fixture/specimen alignment" to "matrix/fibre stress transmission" to "load-bearing fibres", to "failure stage" and to "failure".

Table C.1. Stress and strain values at the end of the transitions occurred during the flexural tests.

Stress and strain at:	PAN				PITCH			
	As-produced		Thermally shocked		As-produced		Thermally shocked	
	μm/m	MPa	μm/m	MPa	μm/m	MPa	μm/m	MPa
Fixture/specimen alignment	135±35	8±3	120±29	7±1	89±2	7±2	87±7	6±1
Matrix-fibre stress transmission	1093±249	82±7	1501±161	104±5	592±180	41±17	765±100	62±14
Load-bearing fibres	2919±642	264±46	2829±431	219±14	2581±67	197±24	1756±123	202±18
Failure stage	3281±717	298±54	3278±606	252±28	3532±172	255±24	3734±282	354±29

Table C.2. Cycle number (#). Residual permanent deformation ($\Delta L_f/L_0$). Relative dimensional change at the maximum temperature ($\Delta L_f/L_0$). Maximum and minimum relative dimensional change ($\Delta L_{\max}/L_0$ and $\Delta L_{\min}/L_0$, respectively). Secant coefficients of thermal expansion (α_1) between the two side temperatures. Polynomial coefficients of first derivative of dilatometric curves (i.e. coefficient of thermal expansion) vs. temperature range 100-1300°C for heating (H0, H1, H2, H3, H4, H5, H6, H7, H8, H9) and cooling (C0, C1, C2, C3, C4, C5, C6, C7, C8, C9). Value of the Young's modulus of the matrix (E_m) extrapolated by fitting the dilatometric curves with Schapery's model having volumetric fibre content fixed at 0.51 and fibre Young's modulus fixed at 780 GPa.

Cycle	PAN				PITCH			
	#1	#2	#3	#4	#1	#2	#3	#4
$\Delta L_f/L_0$ (‰)	0	-0.02	-0.03	-0.03	0	0.11	0.21	0.27
$\Delta L_f/L_0$ (‰)	2.19	2.18	2.18	2.14	2.06	2.12	2.13	2.11
$\Delta L_{\max}/L_0$ (‰)	2.31	2.30	2.28	2.25	2.16	2.22	2.22	2.19
$\Delta L_{\min}/L_0$ (‰)	-0.17	-0.18	-0.18	-0.21	-0.08	0.01	0.08	0.10
α_1 ($10^{-6} \text{ }^\circ\text{C}^{-1}$)	1.81	1.83	1.82	1.79	1.70	1.67	1.59	1.52
H0 ($10^{-6} \text{ }^\circ\text{C}^{-1}$)	17.0739	3.89914	2.71170	3.24947	8.21912	-5.65086	22.6707	4.86525
H1 ($10^{-8} \text{ }^\circ\text{C}^{-2}$)	-10.3490	18.3568	21.2098	19.6745	5.36827	39.2349	-21.5626	14.2115
H2 ($10^{-10} \text{ }^\circ\text{C}^{-3}$)	-1.39597	-26.1009	-28.9020	-27.2499	-12.9788	-45.9856	7.10345	-22.3986
H3 ($10^{-13} \text{ }^\circ\text{C}^{-4}$)	25.6153	138.194	152.058	142.798	72.8557	241.297	-7.73331	123.144
H4 ($10^{-16} \text{ }^\circ\text{C}^{-5}$)	-82.4639	-386.047	-425.159	-395.223	-200.747	-702.34	-7.40573	-354.543
H5 ($10^{-18} \text{ }^\circ\text{C}^{-6}$)	12.9033	63.7584	70.4345	64.5704	31.8642	123.283	2.84104	60.4456
H6 ($10^{-21} \text{ }^\circ\text{C}^{-7}$)	-10.9969	-64.4853	-71.5051	-64.4489	-30.5712	-133.712	-3.05725	-63.3521
H7 ($10^{-24} \text{ }^\circ\text{C}^{-8}$)	4.90419	39.2713	43.7164	38.6270	17.5100	87.6959	1.49090	40.1499
H8 ($10^{-28} \text{ }^\circ\text{C}^{-9}$)	-8.97667	-132.272	-147.819	-127.652	-55.0555	-318.795	-2.68526	-141.293
H9 ($10^{-33} \text{ }^\circ\text{C}^{-10}$)	0	1892.90	2123.61	1786.33	729.472	4930.4	-7.84943	2120.34
C0 ($10^{-6} \text{ }^\circ\text{C}^{-1}$)	-20.3516	-11.2695	-13.7715	-18.4142	-21.1691	-16.5395	-15.2787	-9.43751
C1 ($10^{-7} \text{ }^\circ\text{C}^{-2}$)	3.94175	2.05329	2.53669	3.63834	3.89584	3.08534	2.83224	1.61770
C2 ($10^{-9} \text{ }^\circ\text{C}^{-3}$)	-3.50809	-1.90952	-2.27165	-3.30747	-3.35720	-2.78702	-2.53895	-1.49605
C3 ($10^{-12} \text{ }^\circ\text{C}^{-4}$)	17.5253	10.2366	11.5978	16.7390	16.5230	14.3628	12.9266	8.04044
C4 ($10^{-14} \text{ }^\circ\text{C}^{-5}$)	-5.23141	-3.25115	-3.53131	-5.03218	-4.91620	-4.42892	-3.93593	-2.55737
C5 ($10^{-17} \text{ }^\circ\text{C}^{-6}$)	9.68102	6.33670	6.64723	9.34742	9.11651	8.43426	7.41432	4.97952
C6 ($10^{-20} \text{ }^\circ\text{C}^{-7}$)	-11.1973	-7.66055	-7.80623	-10.8290	-10.5781	-9.98059	-8.69924	-5.99696
C7 ($10^{-23} \text{ }^\circ\text{C}^{-8}$)	7.87279	5.59702	5.56578	7.61403	7.45276	7.13469	6.17964	4.35336
C8 ($10^{-26} \text{ }^\circ\text{C}^{-9}$)	-3.07558	-2.26134	-2.20271	-2.97098	-2.91153	-2.81747	-2.42941	-1.74376
C9 ($10^{-30} \text{ }^\circ\text{C}^{-10}$)	5.11672	3.87475	3.70892	4.93230	4.83312	4.71466	4.05282	2.95756
E_m (GPa)	-	-	-	-	157	144	133	126

Credit authorship statement

P. Galizia: conceptualization, investigation, validation, formal analysis, data curation, writing - original draft - review & editing. **D. Sciti:** project administration, funding acquisition, review & editing